Gomis-Berenguer, A., Celorrio, V., Iniesta, J., Fermin, D., & Ania, C. (2016). Nanoporous carbon/WO3 anodes for an enhanced water photooxidation. Carbon, 108, 471-479. DOI: 10.1016/j.carbon.2016.07.045

Carbon 108 (2016) 471–479

Contents lists available at ScienceDirect

Carbon

journal homepage: www.elsevier.com/locate/carbon

Nanoporous carbon/WO_3 anodes for an enhanced water photooxidation

Alicia Gomis-Berenguer [a], Verónica Celorrio [b], Jesus Iniesta [c], David J. Fermin [b, **], Conchi O. Ania [a, *]

[a] ADPOR Group, Instituto Nacional del Carbon (INCAR, CSIC), 33011 Oviedo, Spain
[b] School of Chemistry, University of Bristol, Cantocks Close, BS8 1TS Bristol, UK
[c] Institute of Electrochemistry, Faculty of Science, Univ. Alicante, 03080, Spain

ARTICLE INFO

Article history:
Received 15 April 2016
Received in revised form
3 July 2016
Accepted 21 July 2016
Available online 22 July 2016

ABSTRACT

This work provides new insights in the field of applied photoelectro chemistry based on the use of nanoporous carbons as additives to tungsten oxide for the photooxidation of water under potential bias. Using a nanoporous carbon of low surface functionalization as additive to WO_3 we have shown the dependence of the photochemical oxidation of water with the wavelength of the irradiation source. Photoelectrochemical responses obtained under monochromatic illumination show a significant increase in the incident photon-to-current conversion efficiency (IPCE) values for electrodes featuring up to 20 wt % carbon additive. Photoelectrochemical transient responses also show a sharp potential dependence, suggesting that the performance of the electrodes is strongly influenced by the carrier mobility and recombination losses. Despite the modest IPCE values of the W/NC electrodes (due to high bulk recombination and poor electron transport properties of the electrodes), our data shows that the incorporation of an optimal amount of nanoporous carbon additive to WO_3 can enhance the carrier mobility of the semiconductor, without promoting additional recombination pathways or shadowing of the photoactive oxide.

1. Introduction

Advances on the use of sunlight as a sustainable low-cost source of energy in various fields have rather been limited to the use of inorganic semiconductors -TiO_2 and metal oxides and sulfides as CdS, Fe_2O_3, or ZnO among most representatives-, that should be stable, nontoxic, inexpensive, and have suitable electronic band positions for an efficient visible light absorption [1–5].

WO_3 is a n-type semiconductor usually presenting a 3D arrangement of slightly distorted corner-shared [WO_6] octahedra compared to the ideal cubic perovskite (type ReO_3), responsible of its electrooptical, electrochromic, ferroelectric and catalytic properties [6–10]. It is considered an interesting visible-light stable photoactive material due to its relatively large abundance, non toxicity, physical and chemical resilience in harsh environments, and most importantly its strong absorption features in the solar spectrum (i.e., band gap between 2.4 and 2.8 eV). The valence band edge of WO_3 is located at approximately 2.9 V vs Ag/AgCl (at pH 0) and is positive enough for the oxidation of water (i.e., high oxidation power of the photogenerated holes). However, the potential associated with the conduction band edge is not negative enough (ca. 0.3 V vs Ag/AgCl) for the reduction of water without a bias voltage. This provokes the surface accumulation of electrons, increasing the recombination rate and ultimately reducing the photoelectrochemical performance of the photoanode [9–13].

To compensate for this limitation of WO_3, several strategies have been adopted such as surface sensitization, optimization of the particle size and morphology control, incorporation of additives and transition/noble metal dopants, or the application in association with suitable photocathodes -i.e. p-type semiconductors-in tandem photoelectrochemical cells [4,14–20]. All these approaches aim to increase the electron trapping by inhibiting the charge recombination.

In this study we have investigated the use of nanoporous carbon additives to WO_3 as an alternative to improve the performance of

* Corresponding author.
** Corresponding author.
E-mail addresses: david.fermin@bristol.ac.uk (D.J. Fermin), conchi.ania@incar.csic.es (C.O. Ania).

http://dx.doi.org/10.1016/j.carbon.2016.07.045

the semiconductor towards the photooxidation of water. Based on the high electronic density of carbon materials, provided by the stacked graphene-layers, it seems reasonable to anticipate that the above-mentioned surface accumulation of electrons can be dissipated by delocalization in the π-electron density of the graphitic structure of carbons. Indeed, the use of carbons of varied nature and characteristics (e.g., carbon nanotubes and nanofibers, graphene, nanoporous carbons, graphitic carbon nitrides) as additives to semiconductors has been widely explored [[21–27] and references therein], and several studies report the enhanced photoconversion yields of such semiconductor/carbon catalysts. In most cases the improved performance is attributed to various phenomena such as: i) an enhanced visible light absorption of the hybrid materials; ii) synergistic effects based on nanoconfinement on the porosity of the carbon support, iii) the strong carbon/semiconductor interfacial electronic effects that favor the reaction with electron donor/acceptors present in the medium. More recently, the photochemical activity of nanoporous carbons has been reported based on the efficient conversion of light into chemical reactions in the confinement of the nanopore space, offering interesting perspectives in different fields [28–35].

Considering all the above, the objective of this work was to explore the effect of a nanoporous carbon as additive to WO_3 in the performance of the resulting hybrid WO_3/NC catalysts for the photooxidation of water. Thus, we provide a systematic investigation of the photoelectrochemical responses of WO_3/nanoporous carbon electrodes for the oxidation of water as a function of the irradiation wavelength, the applied potential bias and the amount of carbon additive. The mixtures were prepared by adding increasing amounts of a nanoporous carbon (ranging from 5 to 80 wt%) to WO_3 powders; the carbon additive was chosen based on its photochemical activity under varied illumination conditions towards the photooxidation of phenol in aqueous solution [28,31].

The novelty of the work is to provide a insight on the role of the carbon additive in the external quantum yield for water oxidation as a function of the carbon ratio, and to correlate the photoelectrochemical response of the WO_3/carbon anodes with the wavelength of the irradiation source. Despite the modest incident photon-to-current conversion efficiency values obtained, our results demonstrate the higher photoconversion values of the photoanodes after the incorporation of the nanoporous carbon, due to the enhanced electron collection provided by the carbon additive. The photoelectrochemical response of the tungsten oxide nanoparticles (severely limited by a poor carrier mobility of the semiconductor) was enhanced by the incorporation of low amounts of the carbon additive; this offers a new approach for the processing of photoelectrodes using low cost nanoporous carbon as sustainable metal-free additives to semiconductors.

2. Experimental

2.1. Materials

The carbon additive (sample referred to as NC) used in the preparation of the WO_3/carbon mixtures is an amorphous nanoporous carbon. Details on the origin and characteristics of this material have been presented in detail elsewhere [26,28]. We herein reintroduce some textural and chemical properties for a better comprehension of the response of the WO_3/carbon photoanodes towards the photooxidation of water. Commercially available WO_3 nanopowders (Fluka, puriss 99.9%, average particle size ca. 40–60 nm, surface pH 4.3) with a monoclinic crystalline structure (JCPDS 01-083-0950), were used as semiconductor.

2.2. Preparation of the electrodes

For the fabrication of the electrodes, about 100 mg of solids (either bare WO_3 or WO_3/carbon mixtures) were dispersed in 750 μL of isopropyl alcohol; about 100 μL of this ink were spread by a micropipette onto an FTO-coated glass slide (surface resistivity ~ 7 Ω/sq) and spin-coated at 3500 rpm for 30 s. The films were dried at 60 °C for 30 min and then annealed at 300 °C for 1 h (heating rate 5 °C/min). The annealing temperature was carefully chosen to avoid modifications in the carbon matrix and semiconductor structure. Indeed, neither the crystallinity of the semiconductor nor the surface chemistry and textural properties of the carbon additive were modified upon the annealing treatment applied in the preparation of the electrodes (see Figs. S1–S3 in the Electronic Supporting Information File, ESI). The WO_3/carbon electrodes will be labeled as W/NCx, were x stands for the amount of nanoporous carbon additive. A series of electrodes containing ca. 5, 10, 20, 50 and 80 wt% of carbon were prepared.

2.3. Photoelectrochemical measurements

Photoelectrochemical measurements were carried out using an Ivium CompactStat potentiostat/galvanostat. The studies were performed in a standard three-electrode system using an electrochemical cell with an optically flat circular quartz window (diameter 2 cm). A Pt wire and Ag/AgCl (saturated KCl) were used as counter and reference electrode, respectively. The prepared electrodes were immersed in an aqueous solution containing 0.5 M Na_2SO_4 (inert electrolyte), previous adjustment of the solution pH to 1.3 by the addition of H_2SO_4. All the experiments were carried out at room temperature. Transient photocurrent responses under on/off illumination cycles were obtained at a constant bias potential between −0.1 and + 0.6 V vs. Ag/AgCl. Current equilibrium at each applied potential was allowed before the irradiation (dark). The electrochemical behavior of the electrodes was also explored by cyclic voltammetry at a potential sweep of 20 mV s^{-1}. The photoelectrochemical responses were measured several times in different electrodes to evaluate the reproducibility; average values corresponding to at least 3 distinct electrodes are presented in this work. Measurements under illumination were performed using a blue LED (Thorlabs) featuring a narrow emission spectrum centered at 371 nm. The LED was powered by a waveform generator (Stanford Research Systems), with a photon flux of 3.4×10^{14} cm^{-2} s^{-1}.). Incident-photon-to-current efficiency (IPCE) at varied wavelengths (ranging between 360 and 460 nm) was measured using 150 W Arc Xe lamp fitted to a single-pass monochromator. The intensity of the irradiation sources was calibrated using a standard silicon photodiode (Newport Corporation). The IPCE values were calculated as:

$$IPCE(\%) = \frac{1240\, j_{ph}}{\lambda P} \times 100$$

where λ (nm) is the wavelength of the monochromatic light irradiating the electrode, j_{ph} (A/cm^2) corresponds to the stationary photocurrent density measured under illumination with P (W/cm^2) incident irradiation. The number 1240 carries the matching units.

2.4. Characterization techniques

The porosity of all the samples was determined by N_2 adsorption/desorption isotherms at −196 °C in a volumetric analyzer (Micromeritics). Before the experiments, the samples were outgassed at 120 °C for 17 h under vacuum (10^{-4} Torr). The specific surface area (S_{BET}), total pore volume (V_{PORES}), and micropore volume (Wo N_2) were obtained from the gas adsorption isotherms.

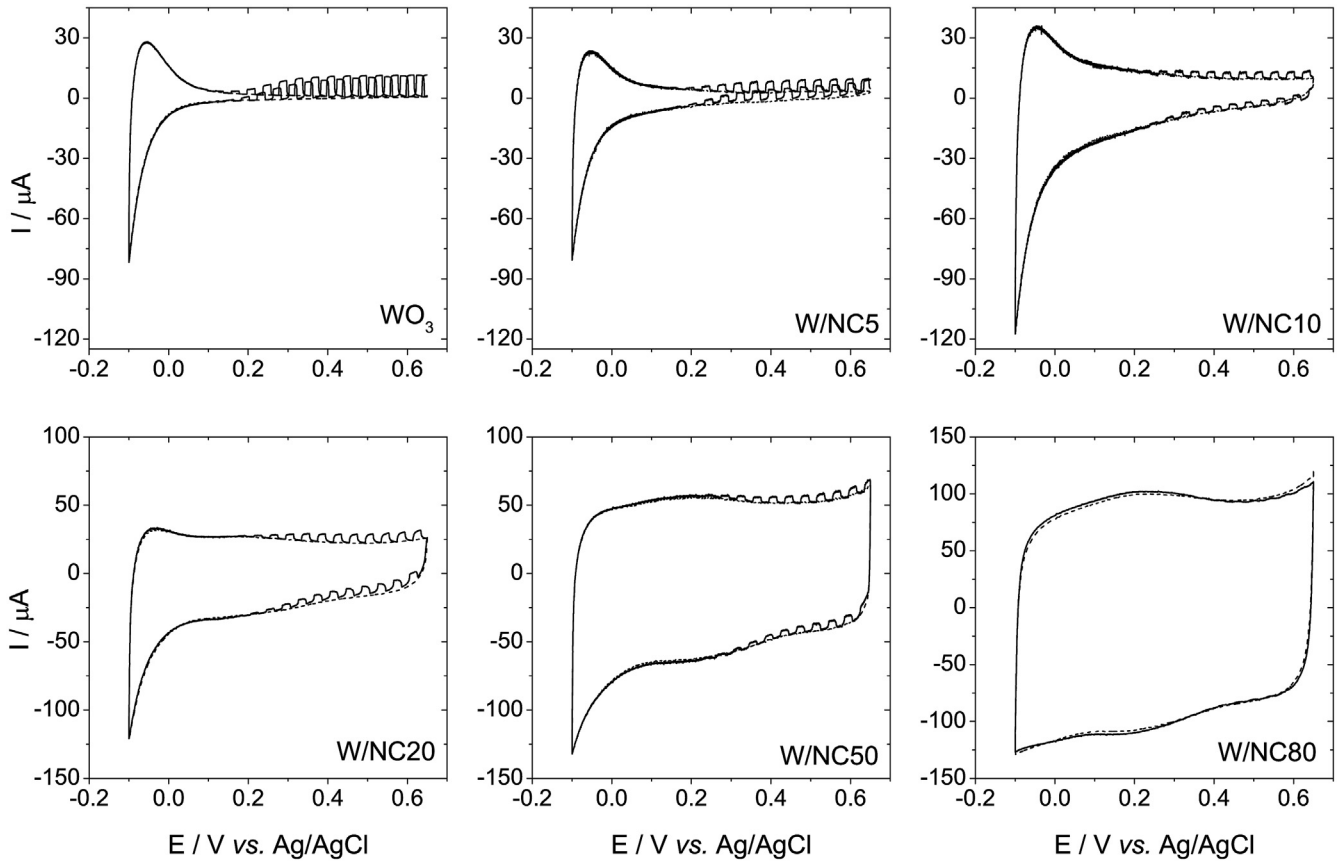

Fig. 1. Cyclic voltammograms, recorded at 20 mV/s, under dark (dashed line) and square-wave light perturbation (solid line) with a frequency of 0.5 Hz in the supporting electrolyte.

Micropore volumes were evaluated using the Dubinin-Radushkevich equation. UV–Vis diffuse reflectance spectra were recorded on a Shimadzu spectrometer (UV-2501) equipped with an integrating sphere and using $BaSO_4$ as a blank reference.

2.5. Electrochemical impedance spectroscopy measurements

Electrochemical impedance spectroscopy (EIS) measurements were carried out in a 3-electrode cell in 0.5 M Na_2SO_4, using WO_3 as working electrode, and a Pt wire and Ag/AgCl (saturated KCl) as counter and reference electrodes, respectively. Potentiostatic EIS measurements were recorded in a potentiostat/galvanostat (VMP-3, Biologic) in the frequency range of 0.01 Hz–100 kHz for selected potentials between −0.6 and + 0.6 V vs. the Ag/AgCl and using 10 mV AC amplitude. Data obtained was fitted to the Mott–-Schottky (MS) equation (see below) that shows the dependence of the interfacial capacitance (C) with the applied potential (E) under depletion conditions (assuming that the dimensions of the semiconductor crystal are larger than the width of the space charge layer), providing useful information about the changes in the charge distribution in the passive layer at the electrode/electrolyte interface.

$$1/C_{CS}^2 = 1/C^2{}_H + 2/\varepsilon\varepsilon_0 eN\left(E - E_{fb} - kT/e\right)$$

where C_{SC} is the charge space capacity, C_H the Helmholtz capacity, N the carrier density (donor $N_D$or acceptor N_A), ε the dielectric constant of the electrode material, ε_0 the electric permittivity of vacuum, *e* the elementary charge, k the Boltzmann constant, T the absolute temperature and E_{fb} the flat band potential.

Table 1
Main textural parameters of the studied photocatalysts obtained from the equilibrium nitrogen adsorption/desorption isotherms at −196 °C.

	S_{BET} [$m^2\ g^{-1}$]	V_{PORES}[a] [$cm^3\ g^{-1}$]	Wo N_2[b] [$cm^3\ g^{-1}$]
WO_3	6	0.038	0.002
W/NC5	56	0.077	0.019
W/NC10	108	0.104	0.037
W/NC20	205	0.160	0.070
W/NC50	524	0.315	0.187
W/NC80	839	0.472	0.279
NC	1033	0.520	0.320

[a] Total pore volume evaluated at p/p_0 ~0.99.
[b] Micropore volume evaluated from the Dubinin-Radushkevich method.

3. Results and discussion

Fig. 1 shows the voltammetric response of the WO_3/carbon electrodes under dark and square-wave light perturbation centered at 371 nm. For WO_3, the voltammograms displayed the characteristic shape of an n-type semiconductor with two distinctive regions (accumulation and depletion) depending on the bias potential. The cathodic current recorded when the electrode potential is swept below 0.1 V vs. Ag/AgCl is attributed to the reduction of the W^{6+} ionic state due to the intercalation of protons and the electrochemical injection of the excess electrons from the substrate to the conduction band of the semiconductor (according to $WO_3 + xH^+ + xe^- \leftrightarrow H_xWO_3$) [36,37]. This charge transfer reaction provokes a blue coloration in the electrode (known electrochromism behavior of WO_3). Upon the reverse scan, WO_3 recovers

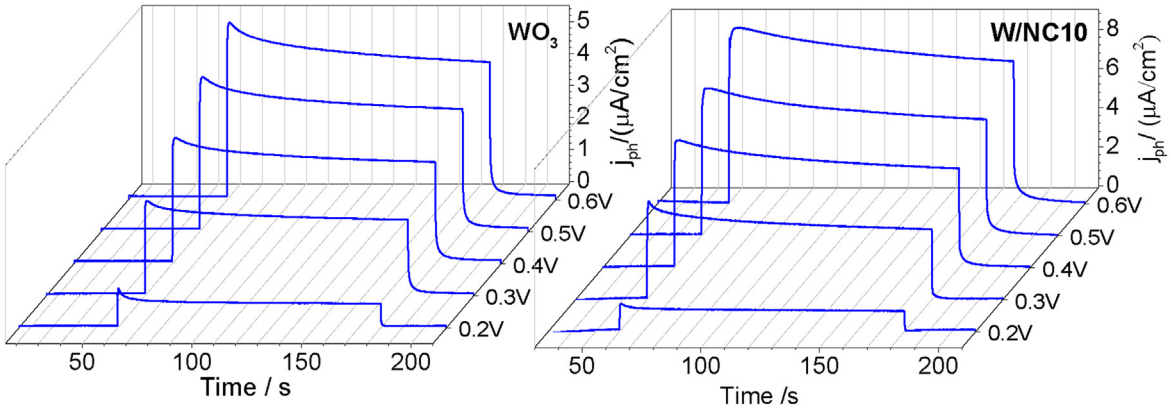

Fig. 2. Transient photocurrent responses of WO_3 and W/NC10 at different bias potentials under illumination (2 min) using a 371 nm LED. (A color version of this figure can be viewed online.)

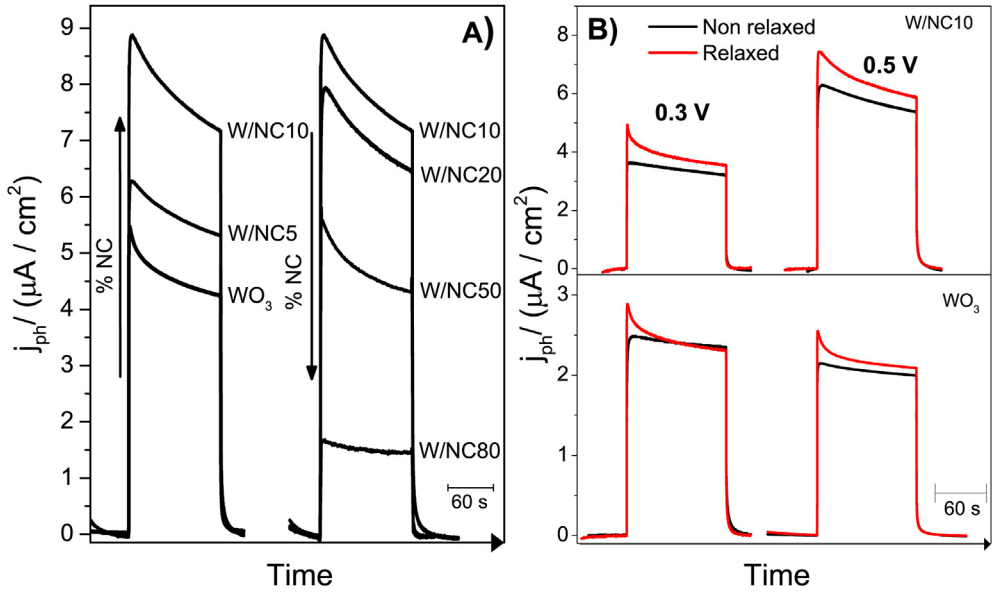

Fig. 3. A) Transient photocurrent responses at 0.6 V vs. Ag/AgCl under illumination (2 min) using a 371 nm LED of the studied electrodes. B) Transient photocurrent at 0.3 V and 0.5 V for WO_3 and W/NC10 electrodes on the second illumination cycle after 0 min (black line) and 5 min (red line) relaxation time between the illumination cycles. (A color version of this figure can be viewed online.)

the translucent-greenish state as a result of the reversible deintercalation of the protons and the simultaneous oxidation of tungsten. Above 0.1 V, the voltammogram exhibits a flat current corresponding to the depletion region where electrons can no longer flow. By expanding the potential window above 1.8 V, an anodic faradaic current appears due to electrochemical decomposition the electrolyte (water oxidation, results not shown).

For the WO_3-carbon electrodes, the capacitive contribution of the nanoporous carbon due to the formation of the electrical double layer is clearly seen in the voltammograms. The current densities under dark conditions gradually increase with the amount of carbon of the electrodes, in agreement with the increasing porous features of the WO_3/carbon mixtures (Table 1, Figs. S4–S6).

In the case of the electrode with the highest amount of carbon (i.e., 80 wt%) it becomes difficult to distinguish the shape associated to the redox reactions at the semiconductor, due to the large capacitive response of the carbon (Fig. S4). Additionally, for this sample, an oxidation/reduction reversible hump is observed close to 0.3 V vs. Ag/AgCl. This is attributed to the pseudo-faradic contribution of the surface groups of the carbon matrix (mainly quinone/hydroquinone pair) [38,39], as the similar behavior is observed in the voltammogram of the nanoporous carbon alone (Fig. S6). Furthermore, the contribution of the double layer capacitance due to the nanoporous carbon allowed verifying the real catalysts composition. Experimental capacitance values measured in all the WO_3/NC electrodes matched the theoretical values corresponding to the amount of carbon additive incorporated to the mixtures (Fig. S5), confirming the homogenous dispersion of the catalysts inks during the preparation of the anodes for all the carbon ratio.

Upon squared-waved illumination at 371 nm, anodic photocurrents were recorded in the voltammetry profiles of all the electrodes, with the exception of W/NC80 (Fig. 1). The electrons in the valence band of WO_3 are promoted to the conduction band and transferred through the bulk semiconductor to the back contact; meanwhile, the holes are transported to the electrode/electrolyte interface where they may react with electron donors present in the

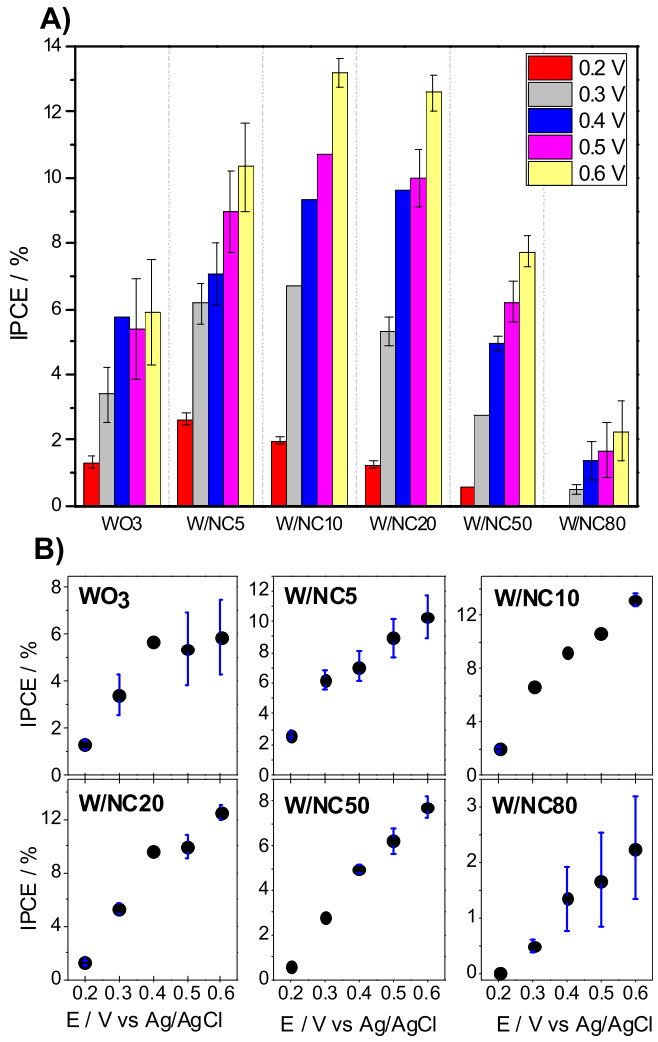

Fig. 4. A) IPCE values of the studied electrodes at different bias potentials upon illumination (2 min) using a 371 nm LED; B) Potential dependence of the IPCE values of all electrodes. (A color version of this figure can be viewed online.)

electrolyte [2,40]. Thus the magnitude of the anodic photocurrent is determined by the rate of water oxidation, the collection of electrons at the back contact and the carrier recombination. The intensity of the photocurrent increases as the potential is swept towards more positive values [2,10].

For n-type semiconductors and in the absence of recombination, the photocurrent onset potential is associated to the flat band potential, which is closed to the conduction band edge [2,41]. The potentials associated with the valance and conduction band edges can be estimated from the potential of electron injection into the conduction band and the optical band gap obtained by diffuse reflectance spectroscopy (Fig. S7). In this regard, the spectrum of bare WO_3 presented the characteristic absorption sharp edge above 470 nm, corresponding to a band gap value of 2.6 eV, in agreement with the values reported in the literature [8–14]. Based on the voltammogram in Fig. 1, the onset potential for electron injection is close to 0.1 V, indicating that the valance band edge is located at around 2.7 V vs Ag/AgCl. These values are also in agreement with those previously reported for this material [8–14]. The characteristic absorption sharp edge of WO_3 was still observed in the diffuse reflectance spectra of the WO_3/carbon mixtures (Fig. S7); the characteristic fingerprint of these spectra suffered a gradual increase in the absorbance in the region between 500 and 800 nm (with the amount of carbon added), due to the strong light absorption features of the carbon component. A similar behavior has been reported for other semiconductor/carbon mixtures (based on TiO_2 and Bi_2WO_6 semiconductors and using carbon nanotubes, activated carbons and carbon hydrochars as additives) [23,25,41–43].

To further evaluate the photoelectrochemical response of the semiconductor we have performed impedance measurements under dark conditions (Mott-Schottky representation is shown in Fig. S8). The dependence of the capacitance values of the space charge region yielded a straight line with a positive slope, characteristic of n-type semiconductors [40] that is inversely proportional to the donor density (N_D). The corresponding value obtained for WO_3 was $N_D = 1.9 \times 10^{20}$ cm^{-3}, which is in good agreement with those reported in the literature for monoclinic tungsten trioxide [14,44]. In the case of the WO_3/carbon mixtures the situation is more complex as the electrochemical impedance is dominated by the large double layer capacitance of the nanoporous carbon (as also seen in Fig. 1), and there is a large incertitude in the values of the dielectric constant of the mixtures.

Fig. 2 shows examples of the photocurrent transients at various potentials for WO_3 and WO_3/NC10 electrodes (data corresponding to all the studied electrodes is shown in Fig. S9). Photocurrent transients were registered for all studied electrodes at different potentials to discriminate the photoelectrochemical response from the capacitive contribution, particularly in the electrodes with the largest amounts of carbon additive.

In all cases, the transient photocurrent curves upon on/off illumination exhibited the characteristic shape of an n-type semiconductor. On switching-on the light, an initial rapid and sharp photocurrent was recorded, followed by a gradual decay as the photogenerated electrons and holes recombine. The current retracted to its original value once the illumination was switched-off instantaneously and it was reproducible during repeated on/off illumination cycles for various electrodes demonstrating the reproducibility and stability of the electrodes under successive cycles; only for higher applied potentials (0.4–0.6 V vs Ag/AgCl) and for electrodes with small carbon loading (ca. 5–20 wt%) a slow decay is observed which we attribute to the stabilization of the electrons in intermediate surface states. The photocurrent onset potential is quite similar in all cases, with a significant increase in photocurrent magnitude in the presence of the carbon additive. It can also be observed that, besides the increase in photocurrent values, the main features on the photocurrent transients remain unaffected by the addition of carbon. On the other hand, the sharp potential dependence of the photocurrent magnitude suggests that the driving force for electron transport is strongly dependent on the position of the electrode Fermi energy. It should be clarified that electron transport is mainly determined by diffusion, given that the nanostructured nature of the oxide prevents the formation of depletion layers [2]. For some electrodes, an initial anodic current peak (overshoot) is observed (Fig. 2, Fig. S9), which is associated to fast recombination processes and complex carrier trapping effects discussed further below.

Fig. 3A shows a direct comparison of the photocurrent transients obtained at 0.6 V vs Ag/AgCl for all the electrodes, to allow a better observation of the effect of the incorporation of the carbon additive. As seen, the photocurrent responses show a sharp increase upon addition of small quantities of carbon, showing the larger value close to 20 wt%. For the electrodes with carbon content of 50 wt% and below, the recorded photocurrent values are higher than those of the bare semiconductor. This is most remarkable considering that the amount of semiconductor is gradually reduces as the amount of carbon additive increases, demonstrating that

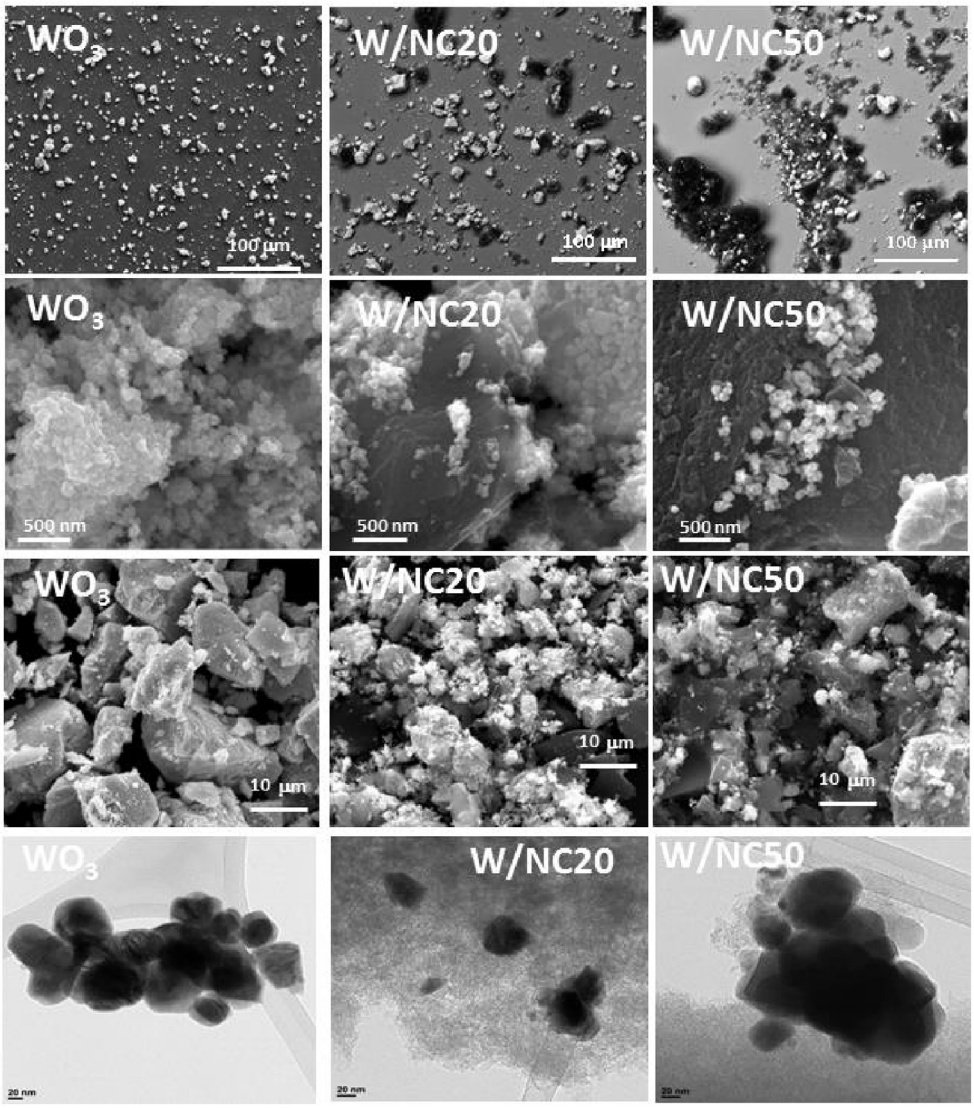

Fig. 5. SEM and TEM images of the some selected photoanodes (first raw) and the catalysts mixtures illustrating the dispersion of the semiconductor and carbon components in the inks.

these W/NC electrodes are more photoactive than bare WO_3. The lower photocurrents of the electrodes with the highest carbon content is most likely due to the lower photogeneration of carriers in the electrodes showing a lower content of WO_3 and to shadowing effects from the carbon additive. Indeed, if the photocurrent responses are normalized by the WO_3 content (Figs. S10 and S11), a plateau for carbon amounts of 20–50 wt% is observed. It is remarkable that even the normalized photocurrent of the electrode W/NC80 is higher than that of bare WO_3 electrode.

The photocurrent decay observed in the transients (Figs. 2 and 3A) originates from a complex relationship between potential distribution across the electrode, trapping of electrons or holes in intermediate surface states and recombination losses (arising from accumulation of holes and electrons at the surface and in the bulk, respectively) [45]. Recombination losses upon accumulation of holes and electrons can be discarded since both phenomena typically manifest by a significantly sharper photocurrent decay accompanied by an equally large cathodic current (undershoot) when the light is turned off (and electrodes in the conduction band react with the accumulated holes). Furthermore, similar photocurrents were obtained by front- and back-side illumination modes of the electrodes, discarding carrier transport limitations as the main mechanism governing the photocurrent losses [46,47]. Hence, the photocurrent decay is most likely attributed to the trapping of electrons in deep states, which leads to a redistribution of the interfacial potential. This process can be regarded as a shift of the effective potential towards more a negative value, promoting a decay of the photocurrent.

Fig. 3B shows the photocurrent transients recorded under consecutive illumination cycles at different time scales. Upon initial illumination, photogenerated electrons are captured by deep trap states, leading to the interfacial potential redistribution mentioned above (Fig. 3B). If a subsequent illumination cycle is allowed before the surface states are emptied, the transient displayed almost a square-shape reaching a stationary photocurrent value. However, if the electrode is kept at open-circuit conditions for 5 min in the dark, the photocurrent transients showed again the gradual fall in the initial photocurrent associated to various trapping states. Similar changes in the population of deep trap states in nanostructured semiconductors in the second time-scale have been

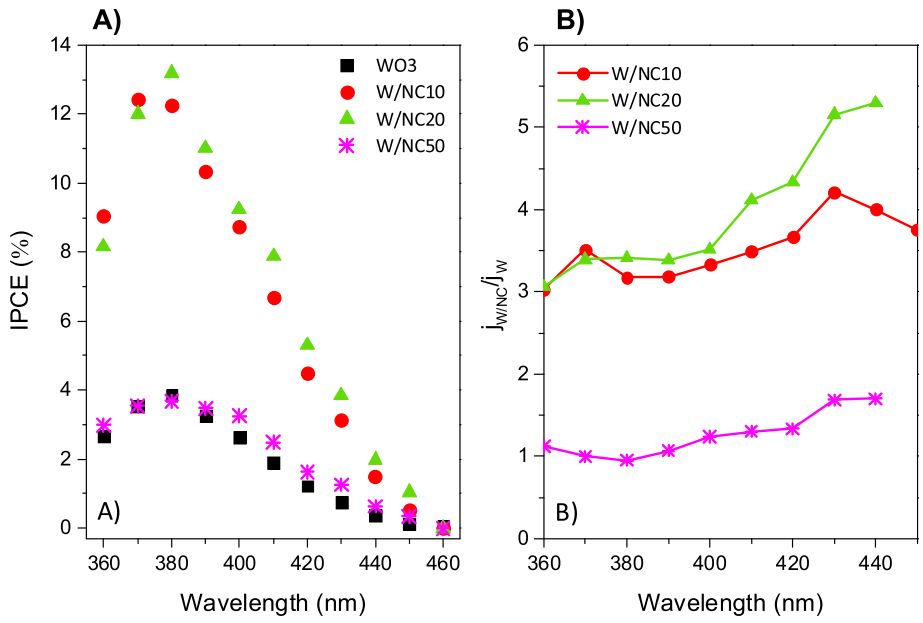

Fig. 6. Dependence of the (A) IPCE values and (B) normalized photocurrent densities ($j_{W/NCx}/j_{WO3}$) with the wavelength of the illumination source (bias potential of 0.6 V, irradiation with a Xe lamp fitted to a single-pass monochromator). (A color version of this figure can be viewed online.)

reported [48].

Fig. 4 represents the IPCE values for all studied electrodes exposed to illumination at 371 nm and bias potentials between 0.2 and 0.6 V vs. Ag/AgCl. Compared to other materials reported in the literature, relatively low IPCE values were obtained for the photoanodes (indicating large current losses resulting in bulk recombination). However it is important to highlight that the IPCE values of the W/NC electrodes are higher than those corresponding to WO_3 at all applied potentials -with the exception of the electrode with the highest carbon loading-.The superior performance of the photoanodes containing the carbon additive confirmed the outstanding role of the nanoporous carbon to achieve a more efficient charge carrier separation of the electrodes. Indeed, the fact that the IPCE values improve for the electrodes containing up to 10–20 wt% carbon (even up to 50% if the normalized photocurrent values by mass of WO_3 are considered) corroborates that there is a more efficient collection of charge carriers in the presence of carbon additive. In other words, the fall in the carrier generation due to decreasing amount of WO_3 in the electrodes is overcompensated by the improvement in the diffusion length of carriers brought about by the carbon additive. Also, IPCE values showed a strong dependence with the bias potential for all the electrodes (Fig. 4B).

Although these IPCE values are not as high as those reported for other water splitting photocatalysts [47], they are most outstanding considering the nature of the carbon additive used in the preparation of the photoanodes (metal-free and amorphous nanoporous carbons).

It should also be pointed out that the preparation of the electrodes has not yet been optimized, thus there should be room for further improvement. In this regard, the dispersion of the semiconductor and carbon particles in the inks is shown in the SEM and TEM images in Fig. 5 and Fig. S12. As above-mentioned, the composition of the inks was homogeneous (Fig. S5) and hence the electrodes were reproducible.

However, the physical mixing of the two components would not seem the optimal method for the preparation of catalysts, since the interaction between both phases is rather weak (dispersive) and largely depends on the formation of aggregates of both component. An improved close contact of the two materials would be expected to facilitates the charge diffusion through the mixture, and hence improving the performance of the electrodes.

To investigate the wavelength dependence of the photochemical response of the electrodes, we recorded the photoelectrochemical response of the anodes under different illumination conditions.

Fig. 6A shows the spectral response of the photocurrent for the W/NC electrodes between 360 and 460 nm. In the case of WO_3, the maximum conversion was recorded at wavelength about 370–400 nm, in agreement with data reported in the literature [49].

The profile of the W/NC photoanodes is very similar to that of bare WO_3. Our previous studies have shown that this nanoporous carbon is photoactive towards the oxidation of phenol in a different spectral range, showing a poor conversion efficiencies at 400 and 450 nm [29], which suggests that different mechanisms apply for these reactions (phenol and water photooxidation). As already observed at 371 nm (Fig. 3A), higher photocurrents were obtained for all the W/NC electrodes, confirming that the effect of the carbon additive applies for a wide wavelength range (and not exclusively in the ultraviolet irradiation). The effect of the carbon matrix is more clearly seen in Fig. 6B, where the photocurrent densities of the W/NC electrodes ($j_{W/NCx}$) are normalized vs that of the bare WO_3 (j_{WO3}). For W/NC10 and W/NC20 the higher values of this ratio are due to the higher efficiency in the photon to current conversions. The profiles show a somewhat constant dependence with the wavelength, with photocurrent densities for W/NC electrodes was found between 3 and 4 times higher than for bare semiconductor for all wavelengths studied (Fig. 6B). The slight increase in the $j_{W/NCx}/j_{WO3}$ ratio over 400 nm, although not very pronounced is significant, and points out that the effect of the carbon additive is higher at wavelengths corresponding to the visible range of the spectrum.

Summarizing, enhanced photocurrent and IPCE values were recorded for the W/NC photoanodes, confirming a more efficient charge carrier collection when the nanoporous carbon additive is incorporated to the electrodes. To understand this behavior we must consider several factors. First of all, the smaller diffusion

length of the minority carriers in nanoporous electrodes (due to the nanometric dimensions of the pore voids) is expected to reduce their recombination, as the carriers easily reach the surface and react with electron acceptors. Secondly, the conjugated π -electron density of the carbon material could act as an acceptor of the photogenerated electrons upon illumination of WO_3, rapidly boosting the electron diffusion via delocalization within the graphene-like sheets. An increased electron diffusion length has already been reported for other semiconductors/carbon materials based on carbon nanostructures with high charge carrier mobility (such as nanotubes and graphenes). For instance, Yousefzadeh and col [50]. described the enhancement in photocurrent density by increasing the MWCNT content from 0 to 1 wt% in the WO_3 films associated to the high electron conductivity, charge transfer and long electron lifetime; more recently Fu and co-workers [51] reported the use of WO_3-reduced graphene oxide nanocomposite showing an enhancement in the photocatalytic performance due to the highly facilitated electron transfer. We herein demonstrate that this behavior can be achieved with a better yield using low-cost nanoporous carbons with a disordered turbostratic structure. In this regard, we have recently reported the visible light driven photoelectrochemical water photooxidation splitting on metal-free nanoporous carbons with varied surface functionalization [30,52,53]. The ability of nanoporous carbons with amorphous structure to oxidize water has been linked to the presence of chromophoric groups and the generation of carriers in reactive sites (associated to surface groups or free edges sites). Moreover, the beneficial effect of carbon additives of varied nature on the photoactivity of WO_3 nanopowders has also been demonstrated for other reactions (i.e., photooxidation of pollutants in aqueous solution) [43,54].

4. Conclusions

WO_3/nanoporous carbon photoanodes were explored to increase the light conversion efficiency of the semiconductor in the photooxidation of water within a wide spectral range. Higher conversion efficiencies in the range of 360–460 nm were obtained upon the incorporation of small amounts of a nanoporous carbon additive, compared to the performance of the bare semiconductor. This is attributed to the improved electron collection provided by the carbon component, which lowers recombination losses, thereby facilitating the oxidation of water at the WO_3/nanoporous carbon/electrolyte interface.

Higher IPCE values were obtained after the incorporation of the carbon additive to the semiconductor; nevertheless, the modest IPCE values and the strong potential dependence of the photocurrent indicate that the recombination and charge collection are still limiting the efficiency. Hence, the possibility of achieving higher conversion efficiencies upon illumination in a wide spectral range using nanoporous carbons with different porous features and conductivity, and the effect of the nanopore confinement on the light propagation for the photoelectrochemical oxidation of water at semiconductor/nanoporous carbon anodes is currently under investigation.

Acknowledgments

COA thanks the financial support of the European Research Council through a Consolidator Grant (ERC-CoG-648161-PHOROSOL) and the Spanish MINECO (grants CTM2014/56770-R, CTQ2013-48280-C3-3-R). VC and DJF kindly thank the UK Catalysis Hub for resources and support provided via the membership of the UK Catalysis Hub Consortium and funded by EPSRC (grants EP/K014706/1, EP/K014668/1, EP/K014854/1, EP/K014714/1 and EP/M013219/1). AGB thanks her PhD fellowship (BES-2012-060410) and VC thanks the UK National Academy and the Royal Society by the support though the Newton International Fellows program.

Appendix A. Supplementary data

Supplementary data related to this article can be found at http://dx.doi.org/10.1016/j.carbon.2016.07.045.

References

[1] A. Fujishima, K. Honda, Electrochemical photolysis of water at a semiconductor electrode, Nature 238 (1972) 37–38.
[2] A.J. Bard, Photoelectrochemistry and heterogeneous photocatalysis at semiconductors, J. Photochem 10 (1979) 59–75.
[3] V.M. Aroutiounian, V.M. Arakelyan, G.E. Shahnazaryan, Investigations of the metal-oxide semiconductors promising for photoelectrochemical conversion of solar energy, Sol. Energy Mater. Sol. Cells 89 (2005) 153–163.
[4] M. Gratzel, Photoelectrochemical cells, Nature 414 (2001) 338–344.
[5] J. He, L. Chen, F. Wang, Y. Liu, P. Chen, C.-T. Au, S.-F. Yin, CdS nanowires decorated with ultrathin MoS2 nanosheets as an efficient photocatalyst for hydrogen evolution, ChemSusChem 9 (2016) 624–630.
[6] J.S.E.M. Svensson, C.G. Granqvist, Electrochromic tungsten oxide films for energy efficient windows, Sol. Energy Mater 1984 (11) (1984) 29–34.
[7] C. Guéry, C. Choquet, F. Dujeancourt, J.M. Tarascon, J.C. Lassegues, Infrared and X-ray studies of hydrogen intercalation in different tungsten trioxides and tungsten trioxide hydrates, J. Solid State Electrochem 1 (1997) 199–207.
[8] X. Liu, F. Wang, Q. Wang, Nanostructure-based WO_3 photoanodes for photoelectrochemical water splitting, Phys. Chem. Chem. Phys. 14 (2012) 7894–7911.
[9] G. Hodes, D. Cahen, J. Manassen, Tungsten trioxide as a photoanode for a photoelectrochemical cell, Nature 260 (1976) 312–313.
[10] S.G. Kumar, K.S.R.K. Rao, Tungsten-based nanomaterials (WO_3 & Bi_2WO_6): modifications related to charge carrier transfer mechanisms and photocatalytic applications, Appl. Surf. Sci. 355 (2015) 939–958.
[11] H. Irie, S. Miura, K. Kamiya, K. Hashimoto, Efficient visible light-sensitive photocatalysts: grafting Cu(II) ions onto TiO_2 and WO_3 photocatalysts, Chem. Phys. Lett. 457 (2008) 202–205.
[12] Y. Nosaka, S. Takahashi, H. Sakamoto, A.Y. Nosaka, Reaction mechanism of Cu(II)-grafted visible-light responsive TiO_2 and WO_3 photocatalysts studied by means of ESR spectroscopy and chemiluminescence photometry, J. Phys. Chem. C 115 (2011) 21283–21290.
[13] Z. Wen, W. Wu, Z. Liu, H. Zhang, J. Li, J. Chen, Ultrahigh-efficiency photocatalysts based on mesoporous Pt–WO_3 nanohybrids, Phys. Chem. Chem. Phys. 15 (2013) 6773–6778.
[14] C.A. Bignozzi, S. Caramori, V. Cristino, R. Argazzi, L. Meda, A. Tacca, Nanostructured photoelectrodes based on WO_3: applications to photooxidation of aqueous electrolytes, Chem. Soc. Rev. 42 (2013) 2228–2246.
[15] W. Luo, T. Yu, Y. Wang, Z. Li, J. Ye, Z. Zou, Enhanced photocurrent-voltage characteristics of WO_3/Fe_2O_3 nano-electrodes, J. Phys. D. Appl. Phys. 40 (2007) 1091–1096.
[16] A. Hameed, M.A. Gondal, Z.H. Yamani, Effect of transition metal doping on photocatalytic activity of WO_3 for water splitting under laser illumination: role of 3d-orbitals, Catal. Commun. 5 (2004) 715–719.
[17] J.M. Spurgeon, J.M. Velazquez, M.T. McDowell, Improving O_2 production of WO_3 photoanodes with IrO_2 in acidic aqueous electrolyte, Phys. Chem. Chem. Phys. 16 (2014) 3623–3631.
[18] G.W. Ho, K.J. Chua, D.R. Siow, Metal loaded WO_3 particles for comparative studies of photocatalysis and electrolysis solar hydrogen production, Chem. Eng. J. 181–182 (2012) 661–666.
[19] K.-S. Ahn, S.-H. Lee, A.C. Dillon, C.E. Tracy, R. Pitts, The effect of thermal annealing on photoelectrochemical responses of WO_3 thin films, J. Appl. Phys. 101 (2007) 093524.
[20] Y. Hou, F. Zuo, A.P. Dagg, J. Liu, P. Feng, Branched WO3 nanosheet array with layered C3N4 heterojunctions and CoOx nanoparticles as a flexible photoanode for efficient photoelectrochemical water oxidation, Adv. Mater 26 (2014) 5043–5049.
[21] C. Huang, C. Chen, M. Zhang, L. Lin, X. Ye, S. Lin, M. Markus Antonietti, X. Wang, Carbon-doped BN nanosheets for metal-free photoredox catalysis, Nat. Commun. 6 (2015) 7698.
[22] G. Zhang, S. Zang, X. Wang, Layered Co(OH)2 deposited polymeric carbon nitrides for photocatalytic water oxidation, ACS Catal. 5 (2015) 941–947.
[23] R. Leary, A. Westwood, Carbonaceous nanomaterials for the enhancement TiO_2 photocatalysis, Carbon 49 (2011) 741–772.
[24] J.L. Faria, W. Wang, in: P. Serp, J.L. Figueiredo (Eds.), Carbon Materials for Catalysis, Ch 13, John Wiley & Sons, New York, 2009, pp. p.481–506.
[25] J. Matos, J. Laine, J.M. Herrmann, Synergy effect in the photocatalytic degradation of phenol on a suspended mixture of titania and activated carbon, Appl. Catal. B Environ. 8 (1998) 281–291.
[26] M. Haro, L.F. Velasco, C.O. Ania, Carbon-mediated photoinduced reactions as a key factor in the photocatalytic performance of C/TiO_2, Catal. Sci. Technol. 2

(2012) 2264–2272.
[27] Y. Zheng, L. Lin, B. Wang, X. Wang, Graphitic carbon nitride polymers toward sustainable photoredox catalysis, Angew. Chem. Int. Ed. 54 (2015) 12868–12884.
[28] L.F. Velasco, I.M. Fonseca, J.B. Parra, J.C. Lima, C.O. Ania, Photochemical response of activated carbons under UV irradiation, Carbon 50 (2012) 249–258.
[29] L.F. Velasco, J.C. Lima, C.O. Ania, Visible-light photochemical activity of nanoporous carbons under monochromatic light, Angew. Chem. 53 (2014) 4146–4148.
[30] C.O. Ania, M. Seredych, E. Rodriguez-Castellon, T.J. Bandosz, Visible light driven photoelectrochemical water splitting on metal free nanoporous carbon promoted by chromophoric functional groups, Carbon 79 (2014) 432–444.
[31] L.F. Velasco, A. Gomis-Berenguer, J.C. Lima, C.O. Ania, Tuning the surface chemistry of nanoporous carbons for an enhanced nanoconfined photochemical activity, ChemCatChem 7 (2015) 3012–3019.
[32] L.F. Velasco, E. Maurino, E. Laurenti, C.O. Ania, Spectroscopic evidence of light-induced generation of radicals on carbon materials, Appl. Catal. A General 453 (2013) 310–315.
[33] T.J. Bandosz, E. Rodriguez-Castellon, J.M. Montenegro, M. Seredych, Photoluminescence of nanoporous carbons: opening a new application route for old materials, Carbon 77 (2014) 651–659.
[34] L. Bao, Z.L. Zhang, Z.Q. Tian, L. Zhang, C. Liu, Y. Lin, B. Qi, D.W. Pang, Electrochemical tuning luminescent carbon nanodots: from preparation to luminescence mechanism, Adv. Mater 23 (2011) 5801–5806.
[35] Q. Bao, J. Zhang, C. Pan, J. Li, C.M. Li, J. Zang, D.Y. Tang, Recoverable photoluminescence of flame-synthesized multiwalled carbon nanotubes and its intensity enhancement at 240 K, J. Phys. Chem. C 111 (2007) 10347–10352.
[36] I. Bedja, S. Hotchandani, P.V. Kamat, Photoelectrochemistry of quantized WO_3 colloids. Electron storage, electrochromic, and photoelectrochromic effects, J. Phys. Chem. 97 (1993) 11064–11070.
[37] C.G. Granqvist, Electrochromic tungsten oxide films: review of progress 1993–1998, Sol. Energy Mater. Sol. Cells 60 (2000) 201–262.
[38] E. Frackowiak, F. Béguin, Carbon materials for the electrochemical storage of energy in capacitors, Carbon 39 (2001) 937–950.
[39] K. Kinoshita, in: Carbon: Electrochemical and Physicochemical Properties, Wiley, New York, 1998.
[40] M.A. Butler, Photoelectrolysis and physical properties of the semiconducting electrode WO_3, J. Appl. Phys. 48 (1977) 1914–1920.
[41] R. Beranek, (Photo)electrochemical methods for the determination of the band edge positions of TiO_2-based nanomaterials, Adv. Phys. Chem. 2011 (2011) 1–20.
[42] J. Araña, J.M. Doña-Rodriguez, E. Tello Rendón, C. Garriga i Cabo, C. González-Diaz, J.A. Herrera-Melián, J. Pérez-Peña, G. Colón, J.A. Navío, TiO_2 activation by using activated carbon as a support: part II. Photoreactivity FTIR study, Appl. Catal. B Environ. 44 (2003) 153–160.
[43] R.J. Carmona, L.F. Velasco, M.C. Hidalgo, J.A. Navío, C.O. Ania, Boosting the visible-light photoactivity of Bi_2WO_6 using acidic carbon additives, Appl. Catal. A 505 (2015) 467–477.
[44] S.R. Biaggio, R.C. Rocha-Filho, J.R. Vilche, F.E. Varela, L.M. Gassa, A study of thin anodic WO_3 films by electrochemical impedance spectroscopy, Electrochimica Acta 42 (1997) 1751–1758.
[45] L.M. Peter, Dynamic aspects of semiconductor photoelectrochemistry, Chem. Rev. 90 (1990) 753–769.
[46] P. Leempoel, Ren F. Fan, A.J. Bard, Semiconductor electrodes. 50. Effect of mode of illumination and doping on photochemical behavior of phthalocyanine films, J. Phys. Chem. 87 (15) (1983) 2948–2955.
[47] S. Xiao, H. Chen, Z. Yang, X. Long, Z. Wang, Z. Zhu, Y. Qu, S. Yang, Origin of the different photoelectrochemical performance of mesoporous $BiVO_4$ photoanodes between the $BiVO_4$ and the FTO side illumination, J. Phys. Chem. C 119 (2015) 23350–23357.
[48] Q. Zhang, V. Celorrio, K. Bradley, F. Eisner, D. Cherns, W. Yan, D.J. Fermin, Density of deep trap states in oriented TiO_2 nanotube arrays, J. Phys. Chem. C 118 (2014) 18207–18213.
[49] C. Santato, M. Odziemkowski, M. Ulmann, J. Augustynski, Crystallographically oriented mesoporous WO_3 films: synthesis, characterization, and applications, J. A. Chem. Soc. 123 (2001) 10639–10649.
[50] S. Yousefzadeh, A. Reyhani, N. Naseri, A.Z. Moshfegh, MWCNT/WO_3 nanocomposite photoanode for visible light induced water splitting, J. Solid State Chem. 204 (2013) 341–347.
[51] L. Fu, T. Xia, Y. Zheng, J. Yang, A. Wang, Z. Wang, Preparation of WO_3-reduced graphene oxide nanocomposites with enhanced photocatalytic property, Ceram. Int. 41 (2015) 5903–5908.
[52] X. Wang, K. Maeda, A. Thomas, K. Takanabe, G. Xin, J.M. Carlsson, K. Domen, M. Antonietti, A metal-free polymeric photocatalyst for hydrogen production from water under visible light, Nat. Mater 8 (2009) 76–80.
[53] Y. Zhao, R. Nakamura, K. Kamiya, S. Nakanishi, K. Hashimoto, Nitrogen-doped carbon nanomaterials as non-metal electrocatalysts for water oxidation, Nat. Commun. 4 (2013) 2390–2397.
[54] R.J. Carmona, L.F. Velasco, E. Laurenti, V. Maurino, C.O. Ania, Carbon materials as additives to WO3 for an enhanced conversion of simulated solar light, Front. Res. 3 (2016) 1–11.